CFD ANALYSIS OF PLASMA FLOW IN A LASER THRUSTER

P. Molina-Morales *, K. Komurasaki†, and Y. Arakawa‡
Department of Aeronautics and Astronautics
University of Tokyo,
7-3-1 Hongo, Bunkyo-ku, Tokyo 113-8656, JAPAN

Abstract

In laser propulsion devices, laser energy is transformed into thermal energy of a propellant gas, producing a so-called laser-sustained plasma (LSP). In this research, laser thruster performance, energy balance and LSP position have all been estimated numerically. A Gauss-Seidel line relaxation scheme has been employed to solve an implicit flux-split difference approximation, yielding results in good agreement with the ones from the experiments. Computational stiffness due to the low Mach number flowfield, present in a large portion of the computational region, has been tackled by applying a CFL number maximization method. Preconditioning, an alternative numerical convergence acceleration method, is also presented in the appendix and its applicability assessed.

Introduction

Considering the increasing demand for the launch of minisatellites into orbit, as well as the development of high power laser systems, laser-heated thrusters represent a promising propulsion concept. One of the laser thruster modes of operation being studied at our laboratory concerns the usage of a continuous-wave CO_2 laser. A schematic of a CW laser thruster is shown in Fig. 1.

Since laser thrusters fly leaving the energy source on the ground, exhaust velocity as well as energy conversion efficiency become of importance. In order to increase the exhaust speed it is necessary to heat up the propellant gas efficiently, requiring the optimization of the laser absorption location inside of the thrust chamber. In the past, numerical and experimental laser thruster research efforts have been done attempting to optimize thruster performance, as documented[1-5] in the reference section.

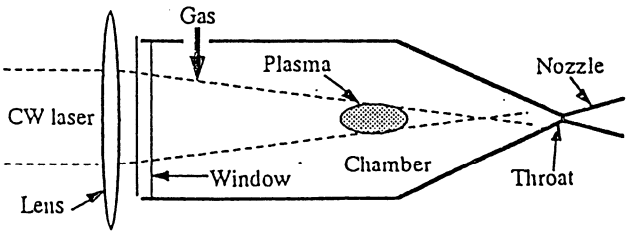

Fig. 1 Laser Thruster Geometry

Concerning the behavior of the laser sustained plasma (LSP), laser energy is absorbed by the propellant gas, with a fraction of this energy being lost energy to the surrounding low temperature gas via 3-D heat transfer. To this respect, a good control of the LSP location is necessary to achieve high exhaust velocities. An accurate analytical model of the LSP thermal processes should eventually enable the establishment of the scaling laws needed for the design of full-scale laser thrusters.

Physical Model

Laser Intensity Distribution

For a laser beam exhibiting a Gaussian profile, the laser intensity distribution can be written as,

*Graduate Student, Department of Aeronautics and Astronautics, University of Tokyo.
†Assistant Professor, Department of Aeronautics and Astronautics, University of Tokyo, Member AIAA/JSASS.
‡Professor, Department of Aeronautics and Astronautics, University of Tokyo, Member AIAA/JSASS.

$$I(x,y) = \frac{2}{\pi}\frac{1}{w(x)^2}\exp\left(-\frac{2y^2}{w(x)^2}\right) \quad (1)$$

Here, x is the axial distance x from the focus, y is the radial distance from the axis and w(x) is the radius location where ω_f can be expressed by $1/e^2$ times the beam intensity on the axis.

$$w(x) = w_f\sqrt{1+\left(\frac{\lambda(x-x_f)}{\pi w_f^2}\right)^2}, \qquad w_f = \frac{2f\lambda}{\pi w_0} \quad (2)$$

The laser beam is divided into 2400 ray flux tubes and Beer's law is applied. Lens aberration and diffraction effects are not considered. Also, although a portion of the plasma radiation is reflected onto the chamber walls of the thruster, this reabsorption effect is negligible and thus ignored.

Inverse Bremsstrahlung Absorption

The propellant gas considered in the present analysis is argon. The absorption coefficient K_{EI} for ion-electron inverse bremsstrahlung given by Kemp[6] is,

$$\frac{K_{EI}}{\rho_p^2} = \frac{1.37x10^{-27}}{T^{1/2}M^2}\lambda^3 G\left(\exp\left(\frac{0.014388}{\lambda T}\right)-1\right) \quad (3)$$

with the Gaunt factor G being

$$G = 1.04 + 3.74x10^{-5}T - 3.28x10^{-10}T^2 \quad (4)$$

The absorption coefficient K_{EN} for neutral particle-electron inverse bremsstrahlung is given in,

$$\frac{K_{EN}}{\rho_p\rho_n} = \frac{9.6x10^{-5}}{M^2}T^2A(T)\lambda^3\left(1-\exp\left(\frac{-0.014388}{\lambda T}\right)\right) \quad (5)$$

Ionization and Recombination Reactions

Single ionization for argon is considered. Although the flowspeed inside of the chamber is quite slow, local thermal equilibrium can be assumed and finite ionization and reaction rates are used. The ionization rate is given by,

$$\omega_f = 1.15x10^{27}T^{-3}\exp(1.81x10^5/T) \quad (6)$$

The recombination rate is determined from the principle of detailed balance using Saha's eq. ,

$$\omega_b = (1/M)(nQ_n/Q_pQ_e)\omega_f \quad (7)$$

The energy equation is defined by considering the ionization energy as the enthalpy for plasma generation and is,

$$E = \frac{p}{\gamma-1} + \frac{1}{2}\rho(u^2+v^2) + \rho_p h_p \quad (8)$$

Radiative Losses

In a laser thruster, radiative losses from the plasma are considered to be the predominant energy loss mechanism. In the present work, the temperature dependence of the radiation intensity is derived from Emmons' experimental results[7]. By using Saha's equation, the dependence on pressure is taken into account.

Heat Conduction

The electron and heavy particle thermal conductivity values for weakly ionized plasmas given by Devoto[8] are used. As plasma diffuses to the low temperature regions, energy transport due to recombination and heat generation takes place. This reactive thermal conduction is obtained by calculating explicitly the diffusion and the ionization/recombination reactions. Concerning plasma diffusion, the following ambipolar diffusion coefficient is used,

$$D \cong \frac{2kT}{Mv} = 4.32x10^{-6}T^{1/2}/(\rho_n+\rho_p) \quad (9)$$

As shown in Fig. 2, the theoretical and experimental thermal conductivity values differ as the gas temperature increases.

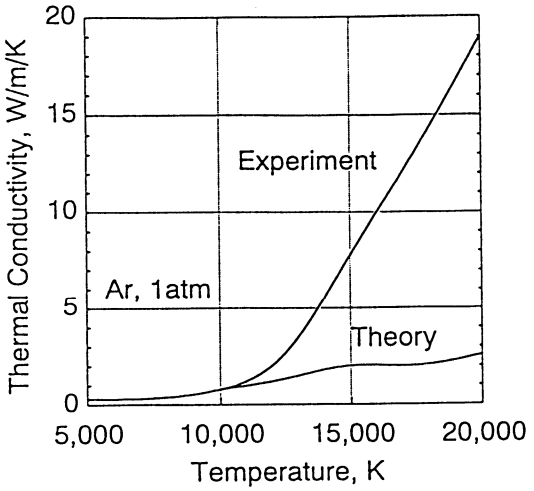

Fig. 2 Theor. & Exp. Thermal Conductivity

This discrepancy is due to short wavelength radiation emanating from the plasma, which is reabsorbed in the low-temperature surrounding region and released as thermal energy. This heat transfer, appearing in the form of radiation, can be approximated by using Fourier's equation[6].

The radiative thermal conduction has been obtained extrapolating the measurements by Emmons[7] (R=5 mm). The radiative thermal conductivity is assumed proportional to the plasma radius (Herein R=1mm).

Convection

Since the propellant is choked at the throat, compressibility effects are important in its vicinity. Also, inside the chamber the gas temperature rises due to laser absorption and large density drops exist. Therefore, compressibility must be considered in the whole flowfield.

We employ an implicit method that allows large maximum timesteps, thus circumventing the stiffness

present in the equations. Another method to speed up numerical convergence called preconditioning has also been investigated and a brief analysis is included in the appendix.

Numerical Method

Governing Equations

In the basic system of equations, compressibility and energy dissipation are considered. Employing the axisymmetric Navier-Stokes equations and using cylindrical coordinates,

$$\frac{\partial U}{\partial t}+\frac{\partial F_I}{\partial x}+\frac{\partial y\, G_I}{y\,\partial y}-\frac{\partial F_V}{\partial x}-\frac{\partial y\, G_V}{y\,\partial y}=W \qquad (10)$$

where

$$U=\begin{bmatrix}\rho_n\\ \rho_p\\ \rho u\\ \rho v\\ E\end{bmatrix},\quad F_I=\begin{bmatrix}\rho_n u\\ \rho_p u\\ \rho u^2+p\\ \rho uv\\ (E+p)u\end{bmatrix},\quad G_I=\begin{bmatrix}\rho_n v\\ \rho_p v\\ \rho uv\\ \rho v^2+p\\ (E+p)v\end{bmatrix}$$

and

$$F_V=\begin{bmatrix}0\\ 0\\ \tau_{xx}\\ \tau_{xy}\\ \tau_{xx}u+\tau_{xy}v+\kappa\partial_x T\end{bmatrix},\quad W=\begin{bmatrix}-\omega_f\rho_p\rho_n+\varpi_b\rho_p^3\\ \omega_f\rho_p\rho_n-\varpi_b\rho_p^3\\ (p-\tau_{\theta\theta})/r\\ 0\\ q\end{bmatrix} \qquad (11)$$

The equation of state is given by,

$$p=(\rho_n+2\rho_p)RT \qquad (12)$$

An upwind discretization method called Flux Vector Splitting[9] is adopted and the governing equations are solved implicitly using a Gauss-Seidel line relaxation method[10]. This overall method is characterized by its robustness and allows large Courant numbers.

Boundary Conditions

At the inlet boundary, total temperature and pressure are stipulated and one more variable is extrapolated from the inside using the upstream Riemann invariant. At the outlet the supersonic exit condition is used, and at the walls the adiabatic and slip conditions are used. Although the boundary layer has some effect on the choked flux, it is not taken into account.

Initial Conditions

Incoming laser beam powers of 400W and 700W are considered, with a laser wavelength of 10.6 μm. As the simulated laboratory model, its throat diameter is 1mm and the angle between the converging wall and the axis is 20°. The total temperature of the propellant gas is 300K and the mass flow is set to either 1.2 or 0.9 g/s. Calculation Courant numbers are 100~300.

Results

Computational Grid and Grid Independence

The computational grid is shown in Fig. 3. For P=700W and a mass flow of 1.2 g/s, the grid independence characteristics, dependent on the maximum temperature and laser absorption, are shown in Fig. 4.

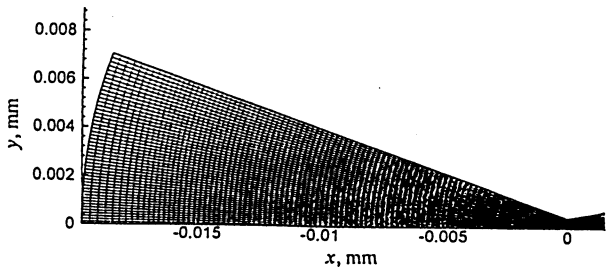

Fig. 3 Computational Grid

In the region were the LSP is generated, if the grid spacing Δy is less than 0.1mm, the introduced error for the values of the maximum plasma temperature and the laser absorption is within 1%. Therefore, a 150x50 grid is deemed sufficient.

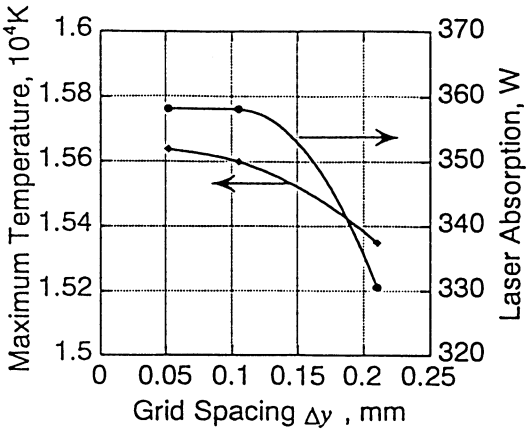

Fig. 4 Grid Independence

Two Dimensional Distribution

Typical temperature and degree of ionization profiles are shown in Figs. 5 and 6. The LSP is generated about 20mm upstream from the focus, the maximum temperature is around 15000K and the degree of ionization is approximately 4%.

Although the plasma close to the throat has fully recombined, near the axis a relatively high temperature is still maintained. Incidentally, in order to obtain a high specific impulse it is necessary to either bring the LSP closer to the throat or increase the laser intensity.

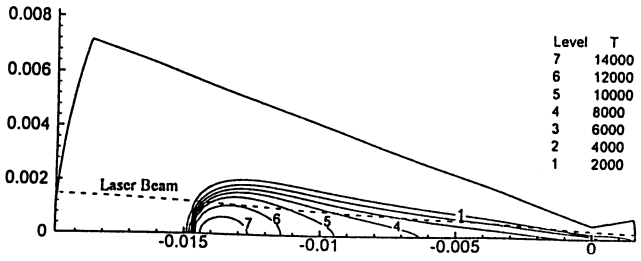

Fig. 5 Temperature Contours

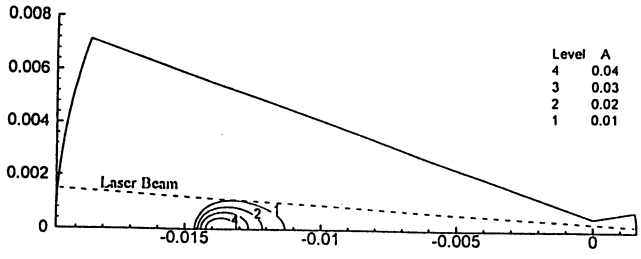

Fig. 6 Degree of Ionization Contours

Furthermore, considering that the propellant gas flowing next to the walls takes most of the heating, it is safe to assume no heat conduction to the wall surfaces. A vector plot of the streamlines and flowfield velocities is shown in Fig. 7. The streamlines are forced around the LSP due to the pressure rise ahead –upstream- of it. Approximately 2-3% of the flow passes through the LSP and rises in temperature due to heat conduction from the LSP. This LSP mechanism can be regarded as analogous to that of a heater.

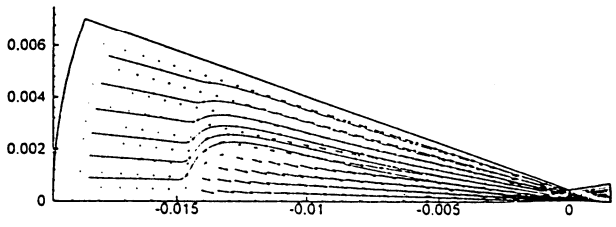

Fig. 7 Streamlines & Velocity Flowfield

Comparison with Experimental Results

The central positions of the LSP obtained from the numerical computation and from the experiments are shown in Fig. 8. The contour where the degree of ionization is 2% was taken as the LSP boundary. In both the numerical and the experimental part, the LSP was generated 8~10mm upstream of the focus for P=400W and 18~20mm upstream of the focus for P=700W.

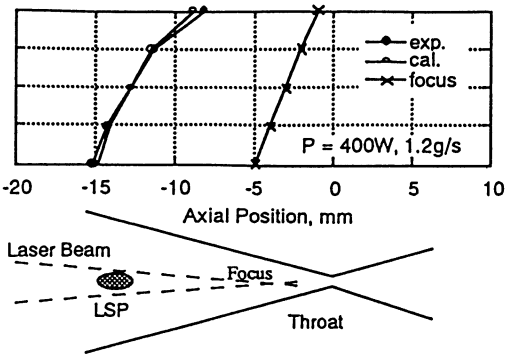

(a) P = 400W, 1.2g/s

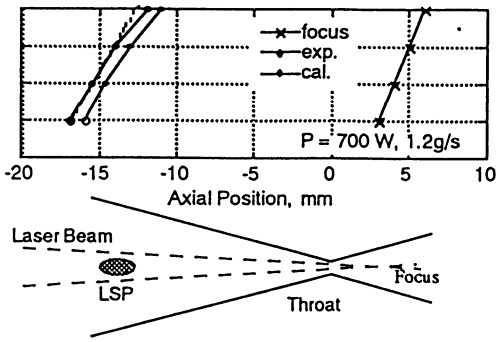

(b) P = 700W, 1.2g/s

Fig. 8 Focus and LSP Location

As the focus is moved downstream, good agreement is obtained in predicting the tendency for the reduction of the distance between the LSP and the focus. In the present simulation code, the coupling of the laser absorption and convective phenomena is well reproduced.

Energy Conversion Efficiency

The thrust measured in the experiments agrees well with the thrust computed assuming proper expansion of the propellant gas from chamber to atmospheric pressure. Values for the thrust and energy conversion efficiency for the numerical and the experimental parts are listed in Table 1.

The mass flow is the same in the numerical part. The values designated with a subscript g indicate the

ones for the case with no laser heating. The values with a subscript $_\infty$ are for the case where the flow in the nozzle expands to vacuum, yielding the ultimate conversion efficiency.

Table 1. Thrust and Energy Conversion Efficiency

	Experiment	Calculation
Chamber Pressure P_c(KPa)	534	534
T/T_∞(mN)	454/681	475/681
Chamber Pressure P_{cg}(KPa)	403	404
$T_g/T_{\infty g}$ (mN)	324/513	336/515
$\eta_T/\eta_{T\infty}$ (%)	8.1/16.1	9.0/15.9

Energy Balance

Based on the data given in Table 1, energy distributions from the experiment and the calculation are shown in Fig. 9. The ultimate energy conversion efficiency based on the thrust is around 16% from both the experimental and the numerical parts. Since the laser absorption fraction obtained from the calculation is 23%, there is a 7% difference. This is considered to be due to the non-uniformity in the velocity distribution of the exhaust jet. This same amount of energy seems to also appear in the experiments as non-recovered energy.

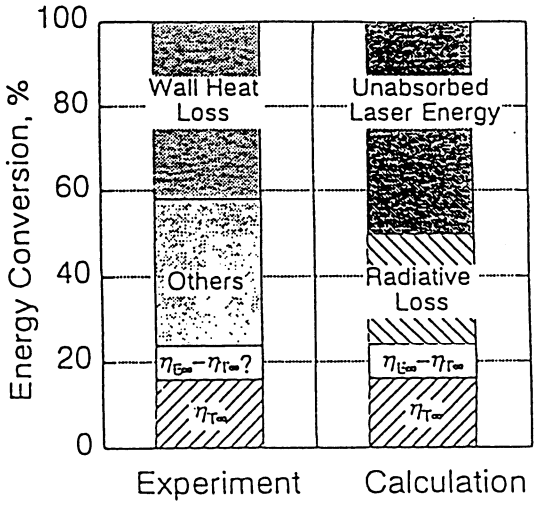

Fig. 9 Energy Distribution

The laser light not absorbed by the propellant gas and the radiation from the plasma fill the inside of the chamber as photon energy. On the wall surface, part of this energy is absorbed and becomes heat loss and the remaining energy either crosses on to the inlet window or travels down the throat. This photon energy loss is thought to be the predominant energy loss mechanism (~75% of input energy) in the laser thruster and perhaps the usage of a regenerative cooling method to recover propellant heat should improve efficiency as well as specific impulse.

Conclusions

A numerical model of the LSP behavior in a laser thruster, dominated by six main physical phenomena (Laser intensity distribution, inverse bremsstrahlung absorption, ionization/recombination reactions, radiation, heat conduction, and convection) has been developed. Using a stable implicit method allowing large timesteps, the problem of stiffness in the system of equations has been circumvented.

Finally, the computed LSP position agreed well with the measured one, implying that the present physical model and the aerodynamic code are suitable for accurate computation. In addition, the energy balance obtained from the numerical analysis was regarded as a new viewpoint for interpretation of experimental results, providing insight necessary for further improvements in thrust performance.

Acknowledgement

The authors gratefully acknowledge the financial support provided by Takahashi Industrial and Economic Research Foundation.

References

[1] **Mead, F.D., Myrabo, L.M. and Messit, D.G.,** Flight and Ground Tests of a Laser-Boosted Vehicle, AIAA Paper 98-3735, Cleveland, OH, 1998.

[2] **Schwartz, S., Mertogul, A., Eguiguren, J., Zerkle, D., Chen, X., Krier, H. and Mazumder, J.,** Laser-Sustained Gas Plasmas for Application to Laser propulsion, AIAA Paper 89-2631, Monterey, CA, 1989.

[3] **Black, J., Krier, H., Glumb, R.J.,** Laser Propulsion 10-kW Thruster Test Program results, J. Propulsion and Power, Vol. 11, No. 6, pp.1307-1316, 1995.

[4] **Keefer, D., Welle, R. and Peters, C.E.,** Power Absorption in Laser-Sustained Argon Plasma, AIAA J., Vol. 24, No. 10, pp. 1663-1669, 1986.

[5] **Girard, M., Lebehot, A. and Campargue, R.,** Numerical Simulation for the Generating Conditions of a Laser-Sustained Argon Plasma Jet, Phys. D: Appl. Phys. 27, pp.253-262, 1994.

[6] **Kemp, N.H. and Lewis, P.F.**, Laser-Heated Thruster-Interim Report, NASA CR 161665, 1980.
[7] **Emmons, H.W.**, Arc Measurement of High-Temperature Gas transport Properties, Phys. Fluids, Vol. 10,, No. 6, pp. 1125-1136, 1967.
[8] **Devoto, R.S.**, Transport Coefficients of Ionized Argon, Phys. of Fluids, Vol. 26, No. 5, pp. 616-623, 1973.
[9] **Candler, G.V. and MacCormack, R.W.**, The Computation of Hypersonic Ionized Flows in Chemical and Thermal Nonequilibrium, J. Thermophysics and Heat Transfer, Vol. 5, No. 3, pp. 266-273, 1991.
[10] **MacCormack, R.W.**, Current Status of the Numerical Solutions of the Navier-Stokes Equations, AIAA paper 85-0032, Reno, NV, 1985.
[11] **Turkel, E.**, Preconditioning Overview, Local Preconditioning Notes.
[12] **Choi, Y.-H. and Merkle, C.L.**, The Application of Preconditioning in Viscous Flows, J. of Comp. Physics, Vol. 105, 1993.
[13] **Turkel, E., Radespiel and Kroll, N.**, Assessment of Two Preconditioning Methods for Aerodynamics Problems, Preprint submitted to Elsevier, November 1997.
[14] **Lee, D., van Leer, B., and Lynn, J.**, A Local Navier-Stokes Preconditioner for All Mach and Cell Reynolds Numbers, Extended Abstract for 13th AIAA Conference on CFD, Snowmass, CO, 1996.

Appendix – Preconditioning Assessment

Laser-sustained plasma flow is characterized by low Mach numbers and low Reynolds numbers. Time-dependent numerical schemes become inefficient because the system of governing equations becomes increasingly stiff, and convergence problems arise. In order to overcome this difficulty, the following two methods are applied in this research: a) Maximizing the implicit CFL number; b) Preconditioning the governing equations. Method a) was employed in the previous section, and in this one a preconditioning method is developed, tested and later compared with method a).

Definition

Preconditioning is a technique devised to remove the stiffness from a system of equations. The convergence of our numerical model to steady-state is impaired for low Mach number regions due to the spread in the characteristic wave speeds, e.g. u, $u+a$, and $u-a$, where u is the total flow speed and a is the speed of sound. The ratio of the largest to smallest wave speed is termed the condition number, κ, and serves as a measure of "stiffness."

Such so-called stiffness takes place in both the subsonic and transonic regions. By plotting the condition number against the Mach number for both the Euler and the preconditioned Euler equations, it can be shown that it is possible to completely eliminate the subsonic stiffness region[11], as well as significantly reduce the transonic stiffness region.

Preconditioning Implementation

In our preliminary computational research, the preconditioned 2-D Euler equations using entropic variables $W = (P,u,v,S)^T$ can be written as

$$\frac{\partial U}{\partial t} + P_r A_r \frac{\partial U}{\partial x} + P_r B_r \frac{\partial U}{\partial y} = 0 \qquad \text{(A.1)}$$

where P_r is the so-called Choi & Merkle preconditioner[12], given in entropic variables by Turkel[13] as,

$$P_r = \begin{bmatrix} \frac{\beta M_r^2}{a^2} & 0 & 0 & -\frac{\beta M_r^2}{a^2} \\ 0 & 1 & 0 & 0 \\ 0 & 0 & 1 & 0 \\ 0 & 0 & 0 & 1 \end{bmatrix} \qquad \text{(A.2)}$$

The eigenvalues of the new system are then,

$$\Lambda_{1,3} = u', u'$$

$$\Lambda_{2,4} = \frac{1}{2}\left[\left(1+\frac{\beta M_r^2}{a^2}\right)u' \pm \sqrt{\left(1+\frac{\beta M_r^2}{a^2}\right)^2 u'^2 + 4\beta M_r^2\left(1-\frac{u^2}{a^2}\right)}\right] \qquad \text{(A.3)}$$

Results

As it can be seen in Fig. 10 for a CFL number of 3, in the preconditioned case convergence is achieved after 1560 implicit iteration steps.

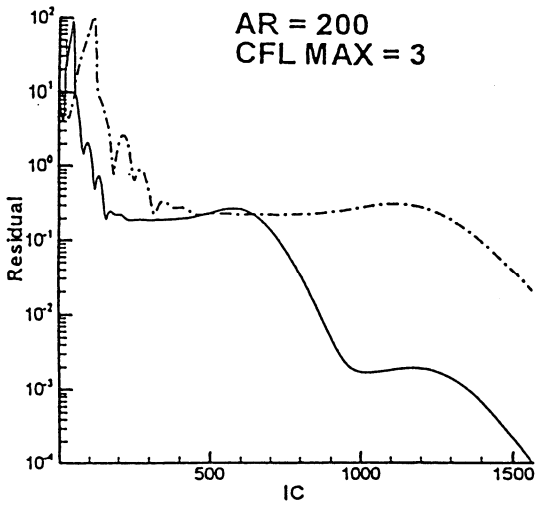

Fig. 10 Convergence History – Preconditioned and Non-preconditioned (dashed line) cases

The non-preconditioned case is shown by the dashed line, which is still far from reaching the same converging level after 1560 iterations. Clearly a significant convergence acceleration is achieved with preconditioning. However, this must be said with guarded optimism, as it was noticed that such acceleration took place for CFL numbers up 3. In other words, it seems that preconditioning imposes a limit on the maximum CFL number.

To this respect, our next step is to attempt to remove this limitation, and therefore a number of points need further consideration.

First, the choice of parameters affecting the preconditioning matrix parameter, namely ß, is a purely educated guess. Depending on the configuration (e.g. airfoil, nozzle, duct with a bump flow) and the initial conditions, this parameter varies greatly. In particular, decreasing ß results in stability problems. A more appropriate definition for the preconditioning matrix parameter which may improve convergence without reducing stability needs to be found.

Second, in a preconditioned system one can frequently see degenerated eigenvectors –nearly parallel eigenvectors- which produce more chances of error during the numerical computation and impose a stability limit. A different preconditioner may yield more optimum eigenvectors.

Third, the preconditioner used in the present work is a low Mach number preconditioner. Perhaps an all-speed preconditioner producing optimal eigenvector orthogonality, such as the one proposed by van Leer[14], may be more suitable for our case.